PAPER

Vapour solid reaction growth of SnO₂ nanorods as an anode material for Li ion batteries†

Kai-Chieh Hsu,[a] Chi-Young Lee[b] and Hsin-Tien Chiu*[a]

Via a vapour−solid reaction growth (VSRG) pathway, phase-segregated SnO₂ nanorods (NRs, length 1−2 μm and diameter 10−20 nm) were developed in a matrix of CaCl₂ salt by reacting CaO particles with a flowing mixture of SnCl₄ and Ar gases at elevated temperatures. The SnO₂ NRs were investigated as a potential anode material for Li-ion batteries (LIBs). A half-cell constructed from the as-fabricated SnO₂ electrode and a Li foil exhibited a reversible capacity 435 mA h g⁻¹ after one hundred cycles at a current density of 100 mA g⁻¹ (0.13 C). The SnO₂ NRs exhibited much better Li storage properties, higher reversible capacity and cyclic capacity retention after extended cycling, than commercial SnO₂ particles did. The improved electrochemical performance is attributed to the presence of an inactive amorphous byproduct matrix, which contains Li₂O, the decomposed electrolyte, and the solid electrolyte interphase (SEI), among the reduced NRs. The matrix probably buffered and reduced the stress caused by the volume change of the electrode during the charge−discharge cyclings.

1. Introduction

Li-ion batteries (LIBs) have been commonly used as a power source for portable electronic devices and are also considered as a candidate to power electric vehicles and hybrid electric vehicles.[1,2] Nanoscale materials are expected to contribute significantly to realizing these important goals in LIB research because the device may achieve high capacity, power rate, and long cycle lifetime simultaneously.[3,4] Graphite is the current choice of anode material for commercial LIBs. However, its theoretical capacity is low, 372 mA h g⁻¹.[5] To achieve high energy density, novel materials are required to replace presently used graphite anodes. Many promising anode electrode materials, such as Si, TiO₂, and Sn-based materials,[6–11] have been explored in order to overcome the limitations. The high theoretically capacity of Sn-based materials are more than twice of that of the commercial graphite. The potential of Li⁺ ion intercalation of Sn-based materials is low. Among them, SnO₂ is regarded as one of the most promising candidates for anode application in LIBs.[12–19] When SnO₂ is used as the active component in the LIBs, the electrochemical reactions are comprised of irreversible and reversible steps, (1) and (2), respectively:

$$SnO_2 + 4Li^+ + 4e^- \rightarrow 2Li_2O + Sn \quad (1)$$

$$Sn + xLi^+ + xe^- \rightleftarrows Li_xSn \ (0 \leq x \leq 4.4) \quad (2)$$
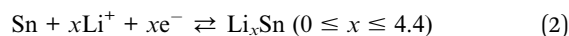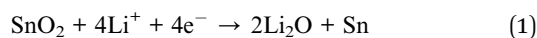
However, these steps provide some drawbacks. Due to its irreversible nature, the first reaction is responsible for the severe capacity loss in the first few cycles. This is the result of the formation of an inactive amorphous byproduct matrix. It probably contains Li₂O, formed from the reduction of SnO₂ by Li, the decomposed carbonate-based electrolyte, and the solid electrolyte interphase (SEI).[20] The second reaction is reversible, with Li⁺ ions repeatedly stored and released during alloying and dealloying cycles. However, a drastic volume change, around 300% during the cyclings, is induced in this step.[21] The so-called pulverization problem blocks the electrical contact pathways and leads to rapid deterioration of the electrode capacity. Unique SnO₂ structures prepared by different synthetic routes could overcome the problem.[14–19] Literature example of electrodes composed of nanoparticles (NPs), one-dimensional (1D), two-dimensional (2D), and hollow nano-structures of SnO₂ showed improved electrochemical performances. These cases, with high surface-to-volume ratio and excellent surface activities, are summarized in Table S1 in the ESI.†

In previous works, we have demonstrated the growths of 1D nanostructures, including as Sn@C core−shell nanowires (NWs), SiC nanotubes (NTs), Si NWs, and graphite fibers, by phase segregation assisted vapour−solid reaction growths (VSRGs).[10,22,23] Solid products generated in a VSRG may interact with others differently. Thus, they do not dissolve each other. Instead, the phase segregation cause the products develop

aDepartment of Applied Chemistry, National Chiao Tung University, Hsinchu 30010, Taiwan, R. O. C. E-mail: htchiu@nctu.edu.tw

bDepartment of Materials Science and Engineering, National Tsing Hua University, Hsinchu 30013, Taiwan, R. O. C.

cooperatively into unique morphology. The observed morphology variations are analogous to the examples found in block copolymer systems.[24,25] In these cases, due to chemical incompatibility, each one of the component blocks self-assembles into nanophases ordered and arranged discretely. In this study, we report a new reaction employing vapor phase $SnCl_4$ and CaO solid particles as the reactants. The products of the VSRG process are SnO_2 and $CaCl_2$ solids. After the removal of the $CaCl_2$ salt, SnO_2 nanorods (NRs) are isolated. Electrodes composed of the SnO_2 NRs are investigated for possible LIB electrode applications. Our observations are discussed below.

2. Experimental

2.1 Growth of SnO_2 nanorods

A typical reaction was carried out inside a hot-wall reactor composed of a Lindberg tubular furnace and a quartz tube (diameter 27 mm). Dehydration of $Ca(OH)_2$ (Sigma-Aldrich) uniformly placed in a quartz boat (length 10 cm) at the centre of the furnace at 1023 K for 1 h produced CaO. $SnCl_4$ (Acros Organics, 99%, anhydrous) was vaporized at room temperature and atmospheric pressure by a flowing stream of Ar (20 sccm) into the reactor and reacted with CaO at a designated temperature and time period. The products were cooled naturally to room temperature in Ar and collected. The products were washed with deionized (DI) water several times to remove the soluble portion. The insoluble portion was dried at 353 K overnight to offer a white product. A summary of the experimental conditions and the obtained products are listed in Table S2 in the ESI.†

2.2 Materials characterizations

Samples were characterized by using a Bruker AXS D8 Advance X-ray diffractometer (XRD) with Cu $K_{\alpha1}$ radiation. Scanning electron microscopic (SEM) images and energy dispersive X-ray (EDX) spectra were taken with a Hitachi S-4700I operated at 15 keV. Transmission electron microscopic (TEM), electron diffraction (ED), high-resolution TEM (HRTEM) images, and EDX data were acquired on a JEOL JEM-2010 at 200 kV.

2.3 Electrochemical tests

Typically, two-electrode 2032 coin-type cells were assembled using the materials described below in a dry room. An N-methyl pyrrolidone (NMP) (Timcal) slurry was prepared by mixing SnO_2, carbon black (Super-P) (Timcal), and polyvinylidene fluoride (PVDF) with a weight ratio 80 : 10 : 10. A Cu foil (Furukawa) (thickness 14 μm), vacuum dried at 403 K overnight, was compressed and cut into disks (diameter 14 mm). An electrolyte composed of $LiClO_4$ (Sigma-Aldrich) dissolved in a mixture of ethylenecarbonate (EC) (Alfa-Aesar) and dimethylcarbonate (DMC) (Alfa-Aesar) (1.0 M, volume ratio 1 : 1) was prepared also. A Li plate was cut into disks (diameter, 14 mm) and used as both the reference and the counter electrode. The amount of the composite was weighed and combined with the electrolyte and the electrodes into coin-type cells. Electrochemical measurements were performed with a battery test system (UBIQ technology, BAT-750B). Cyclic voltammetry (CV) and

electrochemical impedance spectroscopy (EIS) experiments were carried out using a CHI 6081C (CH Instruments) electrochemical analyzer. Electrochemical experiments of the coin-type cells were cycled between 0.005 V and 2.0 V at room temperature. Some of the devices were disassembled after the tests. The composite solids after the cycling were investigated without being washed.

3. Results and discussion

In a horizontal hot-wall quartz tube reactor, $Ca(OH)_2$ powder was dehydrated. As shown by the XRD of the product, CaO was formed (JCPDS card file no. 44-1481 and 70-4068).[25] Then, the as-formed powder was reacted to a flowing mixture of $SnCl_4$ and Ar at 1023 K under atmospheric pressure. After the as-prepared product was washed with DI water to remove $CaCl_2$, the final product sample A, characterized to be SnO_2 NRs as described below, was obtained. Detailed experimental conditions and results are summarized in Table S2 in the ESI.†

3.1 Characterization of SnO_2 NRs

SEM images of sample A are shown in Fig. 1. Fig. 1a displays the typical morphology found A. From a selected area in Fig. 1a,
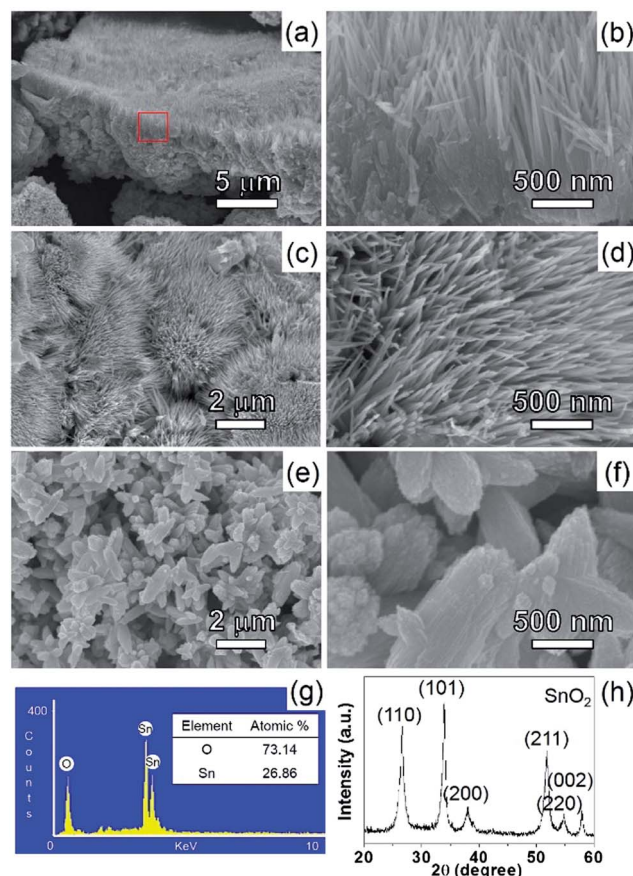

Fig. 1 Low and high magnifications SEM images of A. (a) Sample with both NRs and particles, (b) enlarged view of the squared area in (a), (c and d) views of NRs, and (e and f) views of particles. (g) EDX and (h) XRD pattern.
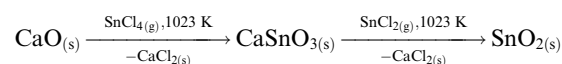
numerous NRs (diameter 10–20 nm, length 1–2 μm) on top of an aggregate of particles can be seen in the magnified view in Fig. 1b. Fig. 1c and d display the views on top of the NRs. Fig. 1e and f present the low and high magnification views of representative aggregates of particles, respectively. From TEM studies (see below), the particles are characterized to be composed of bundles of NRs. An EDX of sample A shown in Fig. 1g indicates that it contains both Sn and O. The XRD pattern in Fig. 1h confirms that sample A is composed of SnO_2 (JCPDS card File no. 41-1445).[26] Another type of less observed morphology, shown in Fig. S1 in the ESI,† also presents bundles of branched NRs. The estimated amount of this morphology is *ca.* 5%.

TEM studies of sample A are shown in Fig. 2. In Fig. 2a, the image of a 1D material is presented. Its length, 150 nm, suggests that it is a fragment of a NR. It confirms that the NR structure with diameter 7–20 nm are observed shown. The SAED in Fig. 2b shows a dot pattern. This indicates that the sample can be indexed to the [0 1 0] zone axis of the single crystalline SnO_2. From the image, the lattice parameters *a* and *c* of a tetragonal crystal system are estimated to be 0.47 nm and 0.31 nm, respectively.[26] Fig. 2c shows a high resolution lattice image of the sample displayed in Fig. 2a. The space between the parallel fringes from the crystalline structure was measured to be 0.24 nm and 0.27 nm. These are equal to the spacings of the {2 0 0} and {1 0 1} planes of SnO_2, respectively. Also, the image suggests that the diameter of the NR is 18 nm. Combined with the SAED result, the crystallization of the NR is determined to be along the [0 0 2]. Fig. 2d displays the image of a particle found in sample A. The magnified view of a selected area shown in Fig. 2d is presented in Fig. 2e. From the image, it is clear that the particle is actually composed of bundles of numerous NRs with gaps among them. The SAED of the selected area displays a slightly diffused dot pattern which can be indexed to SnO_2 also.[26] This suggests that all NRs in the bundles are single crystalline, with the same crystallization orientation but independent from each other in space. Thus, voids exist among the
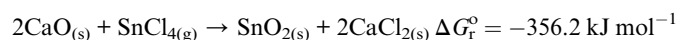
NRs. According to a literature report, the volume change is about 300% during the cyclings.[21] By assuming that the length of the NR does not increase during the cyclings, the diameter would increase about 75% at most. These gaps or voids may act as the buffer areas to accommodate the volume expansion of the electrode material during Li alloying and dealloying processes.[14,15] Details will be discussed more below.

3.2 Proposed reaction pathway

To understand more about the factors affecting the NRs growths, several samples prepared at different reaction conditions were investigated. Sample B was the as-synthesized product formed at 1023 K without DI water washing. The co-existence of SnO_2 and $CaCl_2$ was observed by SEM, EDX and XRD, as shown in Fig. S2 and S3 in the ESI.† SEM and XRD characterizations of samples C, D and E are displayed in Fig. S3–S5.† In samples C and E, prepared by using a shorter reaction time or a lower temperature, respectively, than the condition employed to form sample A, the coexistence of SnO_2 and $CaSnO_3$ is found. We attribute $CaSnO_3$ as an observed intermediate and describe the overall reactions in the equation below.

$$CaO_{(s)} \xrightarrow[-CaCl_{2(s)}]{SnCl_{4(g)}, 1023\,K} CaSnO_{3(s)} \xrightarrow[-CaCl_{2(s)}]{SnCl_{2(g)}, 1023\,K} SnO_{2(s)}$$

The overall reaction stoichiometry is proposed to be:

$$2CaO_{(s)} + SnCl_{4(g)} \rightarrow SnO_{2(s)} + 2CaCl_{2(s)}\ \Delta G_r^o = -356.2\ kJ\ mol^{-1}$$

The reaction is thermodynamically favoured due to the negative standard Gibbs free energy of reaction ΔG_r^o.[27] In addition, we suggest that SnO_2 NRs are grown *via* a VSRG pathway similar to the one proposed for the growths of nanosized graphite and Si crystals with various mophologies.[23] The overall phenomena resembled the morphology alterations caused by the phase segregation in block copolymer systems.[24,25] In this study, the initial products were $CaSnO_3$ and $CaCl_2$. Further reactions between the $SnCl_4$ vapour and the $CaSnO_3$ solid would produce a molten mixture of SnO_2 and $CaCl_2$. The solubility of the high melting point SnO_2 (mp 1903 K) in the low melting ionic $CaCl_2$ (mp 1045 K) is expected to be extremely low. As the reaction prolongs, SnO_2 crystallizes into the NR shape in the molten $CaCl_2$. These are summarized in Scheme 1.

3.3 Electrochemical properties of SnO_2 NRs

Half-cells composed of a Li foil, as the negative electrode (anode), and SnO_2 NRs, as the positive electrode (cathode), were assembled into test cells for the following electrochemical studies. To understand the electrochemical reactions during the cell cycling, CV measurements were performed and presented in Fig. 3a. In the first cathodic sweep, a broad peak at 0.59 V is attributed to the reduction of SnO_2 to form Sn, as described in eqn (1), and the formation of the SEI layer.[28,29] In the following cycles, the peak disappears while two peaks, at
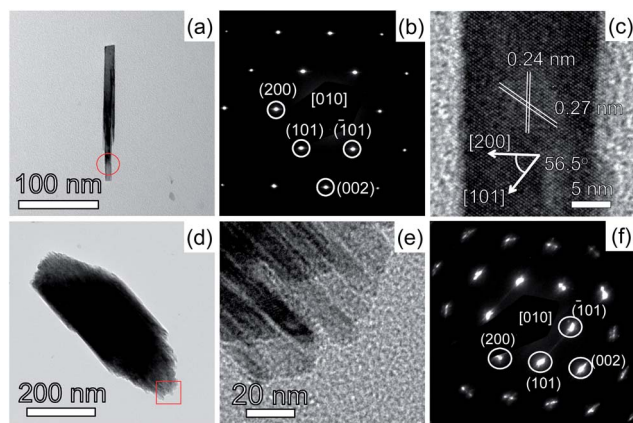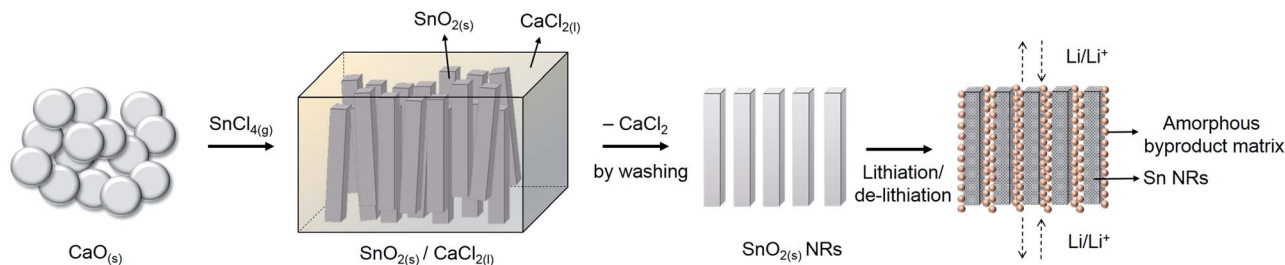

Fig. 2 TEM studies of A. (a) Image of a section of a NR, (b) SAED pattern, and (c) HRTEM image from the circled area in (a), (d) a bundle of NRs, (e) high magnification image, and (f) SAED pattern from the squared area in (d).

Scheme 1 Proposed VSRG pathway to form SnO_2 NRs and schematic diagram showing the role of the amorphous byproduct matrix during the lithiation and de-lithiation.
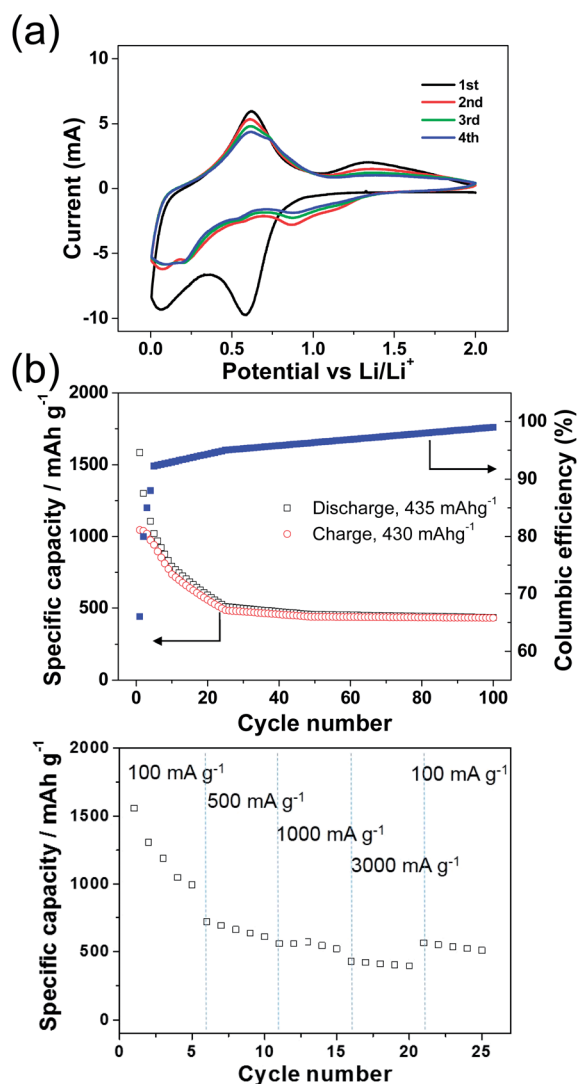

Fig. 3 (a) CV of a SnO_2 NR electrode scanned at 0.5 mV s^{-1}. (b) Specific capacity and columbic efficiency of a SnO_2 NR electrode cycled at 100 mA g^{-1}. (c) Discharge capacity of a SnO_2 NR electrode as a function of discharge rate (100–3000 mA g^{-1}). All experiments were cycled between 0.005 V and 2.0 V vs. Li/Li$^+$.

0.88 V and 1.15 V, are observed. Another peak at 0.07 V is found in the first cycle. It shifts slightly in the subsequent scans to 0.2 V with reduced peak current. The observations are attributed to

the occurrence of irreversible processes initially and the formation of various Li$_x$Sn alloys, as suggested by eqn (2), during the cathodic sweeps.[30,31] In the anodic sweeps, two peaks are found. The one at ca. 0.61 V is assigned to the dealloying process of Li$_x$Sn, the reverse reaction in eqn (2). The other peak is at ca. 1.34 V, which is associated with partial oxidation of Sn to form tin oxides. The signal corresponds to a small peak at ca. 0.55 V in the cathodic scans, indicating the reduction of the oxides to Sn metal.[28] Fig. 3b depicts the specific capacity and the columbic efficiency of the discharge–charge process of the half-cell with a cycling rate 100 mA g^{-1} (0.13 C). The first discharge and charge steps deliver specific capacities 1583 and 1044 mA h g^{-1}, respectively. The large initial capacity loss can be attributed to the reduction of SnO_2 to form Sn, the formation of the SEI layer on the electrode surface during the first discharge step, and the storage of Li$^+$ ions in the EC/DMC-based electrolytes.[28–31] These materials are attributed to the major components in the inactive amorphous byproduct matrix formed among the NRs and will be discussed more below. Obviously, the capacity dropped swiftly for the first twenty five cycles. In the later cycles, the specific capacity and the columbic efficiency stay relatively stable. At the end of the one hundredth cycle, a respectable specific capacity 435 mA h g^{-1} and a columbic efficiency over 98% are observed. In contrast, the cycling performances of half-cells constructed from commercial SnO_2 powders (particle sizes 1–10 μm and 100 nm) at 100 mA g^{-1} are poor, as shown in Fig. S6a in the ESI.† Fig. S6b† displays the discharge capacities of the device fabricated from SnO_2 NRs at high current rates 500, 1000, and 3000 mA g^{-1} (0.63, 1.26 and 3.78 C). After one hundred cycles, the discharge (Li alloying) capacities are found to be 357, 290 and 215 mA h g^{-1}, respectively. In Fig. 3c, a capacity 997 mA h g^{-1} is observed after the battery is cycled at 100 mA g^{-1} for five times. Then, after it is cycled at 500 mA g^{-1}, 1000 mA g^{-1}, and finally 3000 mA g^{-1} for five times each, the half-cell shows a capacity 510 mA h g^{-1} at 100 mA g^{-1}, very close to value found in the twenty fifth measurement shown in Fig. 3b, 518 mA h g^{-1}. These observations demonstrate that even after the fast discharge–charge cycles at 3000 mA g^{-1}, the electrode did not degrade severely so that the half-cell still exhibited excellent cycling properties.

Clearly, the half-cells constructed from the SnO_2 NRs demonstrate much better performance than the ones from the commercial SnO_2 powders do. To understand the alteration of the electrode material after repeated lithiation and de-lithiation

processes, a SEM image of the electrode after one hundred discharge–charge cycles is shown in Fig. 4a. Clearly, many NRs still maintain their original 1-D morphology when they are compared to the image of the original electrode shown in Fig. 4b. In addition, the EDX and the XRD data of the electrode material after one hundred cycles are displayed in Fig. S7 in the ESI.† The EDX spectra in Fig. S7a† suggest that both Sn and O atoms are the major components of the electrode. The XRD pattern in Fig. S7b† indicates the presence of Sn and Cu metals, which is the foil for the electrode contact. This suggests that the SnO$_2$ NRs has been completely converted into Sn metal NRs during the discharge–charge cycles. Based on the results, we assign the O signal found in the EDX to Li$_2$O, formed from the reduction of SnO$_2$ by Li, the irreversible decomposition of the electrolyte, and the SEI layer on the surface of the active material formed during the cell cyclings.[20,28–33] Due to its light mass, Li cannot be observed by EDX. These inactive components appear to be amorphous because no related XRD signals can be found in Fig. S7b.† We assume that the amorphous byproduct matrix played an important role for maintaining the cell performance over extended discharge–charge cycles.[33] The soft and low density matrix appears to intersperse uniformly among the NRs. The separations could effectively minimize the aggregation of the as-formed Sn NRs. Also, due to the even distribution of the voids among the inactive matrix, the mechanical stress caused by the volume changes in the lithiation and de-lithiation process could be alleviated, as shown in Scheme 1. In contrast, the electrode fabricated from commercial SnO$_2$ show severe aggregations after fifty discharge–charge cycles, as demonstrated in the SEM image shown in Fig. S8 in the ESI.†

Considering a relatively wide voltage window applied in this study, we summarize the enhanced capacity of the SnO$_2$ NRs based cells at long cycles and variable rates to the following reasons. First of all, the amorphous byproduct matrix in the voids among the NRs might effectively buffer the drastic volume changes during the lithiation and de-lithiation process. Also, due to the presence of the matrix, the NR structure was maintained after SnO$_2$ was reduced to Sn. The NR structure may provide effective electrolyte/electrode contact surfaces which shorten the transport lengths for both electrons and Li$^+$ ions. In addition, the diffusion time of ions could be reduced in the nanocomposite so that the rates of phase transitions are increased.

To understand the effect of the SnO$_2$ morphology on the electrochemical performances further, EIS studies were carried out.[34,35] As shown in Fig. 5a, the EIS spectra of the half-cells constructed from the NRs and the commercial powder of SnO$_2$ exhibit typical Nyquist plots. Each one consists of a high frequency semicircle (100 kHz to 10 Hz) and a low frequency inclined line (10–0.1 Hz). The high frequency semicircle represents the charge transfer resistance of the electrochemical reactions across the interface between the electrolyte and the electrode surface, and the contact resistance among the components on the electrode. The semicircle from the SnO$_2$ NRs-based cell shows a smaller diameter, implying its better electrochemical performance.

To quantify the experimental EIS results, the spectra were fitted with the equivalent electrical circuit shown in Fig. 5b.[35] It consists of a serial connection of R_e, $R_{(sf+ct)}$ + W//CPE, and R_f//C. Here, R_e is the electrolyte resistance, $R_{(sf+ct)}$ is the surface film
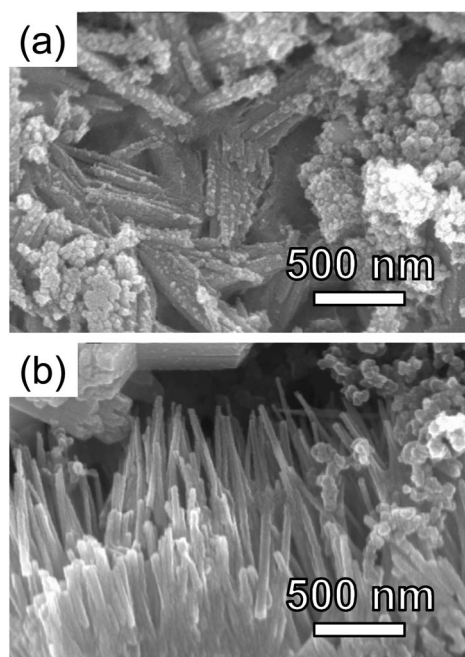

Fig. 4 SEM images of (a) an electrode after one hundred cycles of lithiation and de-lithiation (without being washed) and (b) the original SnO$_2$ NR electrode. The electrode was fabricated from a mixture of SnO$_2$ NRs, carbon black, and binder.
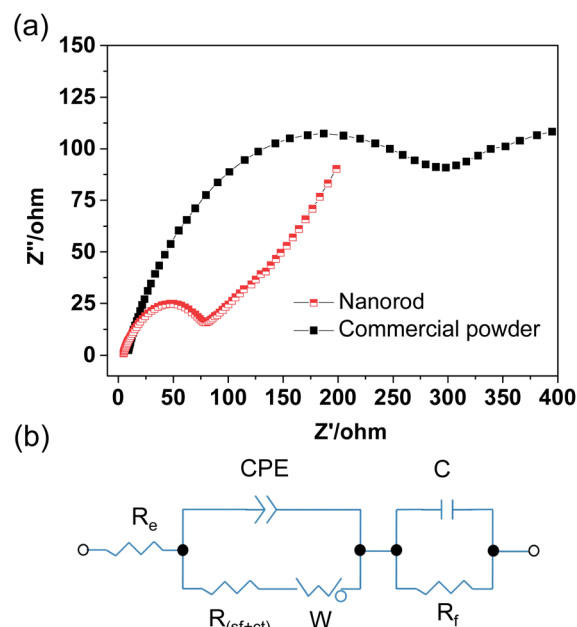

Fig. 5 (a) Nyquist plots from coin cells composed of as-fabricated NR and commercial powder of SnO$_2$. (b) Equivalent circuit for experimental data fitting. R_e: electrolyte resistance; $R_{(sf+ct)}$: surface film and charge transfer resistance; R_f: polarization resistance; CPE: constant phase elements; W: Warburg impedance; C: intercalation capacitance.

Table 1 Fitted impedance parameters obtained from EIS using the circuit in Fig. 5b

Electrode materials	R_e (Ω)	$R_{(sf+ct)}$ (Ω)	CPE (μF)	R_f (Ω)	C (μF)
NR	3.0	81	488	22	8
Commercial powder	5.0	424	2493	111	4

and charge transfer resistance, R_f is the polarization resistance, CPE (constant phase element) is the indicator for the roughness, porosity, and inhomogeneity of the electrode surface, W is the Warburg impedance, and C is the intercalation capacitance. The fitted results are listed in Table 1. $R_{(sf+ct)}$ of the cell value 81 Ω while the cell constructed from the commercial powder is high, 424 Ω. The observation implies that in the cell fabricated from the SnO_2 NRs, the charge transfer and Li^+ ion fabricated from the SnO_2 NRs exhibit a low diffusion pathways are efficient. Thus, the enhanced electrode performance can be attributed to the presence of the LiO_2/Sn NRs nanocomposite structure which not only enhances the diffusion and the charge transfer but also buffers the large volume changes during the discharge–charge cycles.

4. Conclusions

In summary, SnO_2 NRs have been prepared in high yields by a simple and unique process. By reacting $SnCl_4$ vapour with CaO solid, SnO_2 NRs are formed via VSRG pathway. The crystallization of SnO_2 in the phase segregated molten salt of $CaCl_2$ assists the growth of the NRs. The half-cells fabricated from SnO_2 NRs morphology perform much better than the ones constructed from featureless commercial SnO_2 particles do. When SnO_2 NRs are reduced by Li in the cell, Sn NRs embedded in the inactive amorphous byproduct matrix are produced. The nanocomposite provides short diffusion lengths, efficient Li^+ ion transport, and improved charge transfer. The amorphous byproduct matrix assists maintaining the original morphology by reducing the aggregation of the NRs. The matrix also provides space to buffer the large volume changes of the electrode material during the discharge–charge cycles. As a result, the cycling performance of the electrode fabricated from the SnO_2 NRs improves significantly over that of the one constructed from the commercial SnO_2. In addition, performance of the device fabricated from our SnO_2 NRs is comparable to and exceeds many literature cases shown in Table S1 in the ESI.† For example, performances of the cells constructed from SnO_2 NTs, NWs, and NPs are 250, 210, and 90 mA h g^{-1}, respectively, after fifty cycles at 100 mA g^{-1}.[14] For comparison, the value of the cell fabricated from the SnO_2 NRs reported in this study is 456 mA h g^{-1} after the same number of cycles at the same rate. In another example, a cell made from SnO_2 nanosheets shows a capacity 559 mA h g^{-1} after twenty cycles at 78.2 mA g^{-1} (0.1 C).[18] The result of the cell fabricated in this study is 591 mA h g^{-1} after twenty cycles at 100 mA g^{-1}. Lastly, a cell constructed from SnO_2 hollow nanospheres retains a capacity 450 mA h g^{-1} after 40 cycles at a rate 130 mA g^{-1} (0.2 C).[19] The performance of the cell constructed from our NRs is, as mentioned above, 456 mA h g^{-1} after fifty cycles at 100 mA g^{-1}. At the end of the one hundredth cycle, the specific capacity is 435 mA h g^{-1}. Recently, sandwich-stacked SnO_2/Cu hybrid nanosheets have been developed to demonstrate even better performance.[36] We anticipate that by coupling our SnO_2 NRs with other well-designed cell structures, further LIB performance improvements may be realized.

Acknowledgements

Notes and references

1 J.-M. Tarascon and M. Armand, *Nature*, 2001, **414**, 359.
2 B. Scrosati and J. Garche, *J. Power Sources*, 2010, **195**, 2419.
3 A. S. Aricò, P. Bruce, B. Scrosati, J.-M. Tarascon and W. Van Schalkwijk, *Nat. Mater.*, 2005, **4**, 366.
4 P. G. Bruce, B. Scrosati and J. M. Tarascon, *Angew. Chem., Int. Ed.*, 2008, **47**, 2930.
5 M. Winter, J. O. Besenhard, M. E. Spahr and P. Novak, *Adv. Mater.*, 1998, **10**, 725.
6 C. Yu, X. Li, T. Ma, J. Rong, R. Zhang, J. Shaffer, Y. An, Q. Liu, B. Wei and H. Jiang, *Adv. Funct. Mater.*, 2012, **2**, 68.
7 N. Liu, H. Wu, M. T. McDowell, Y. Yao, C. Wang and Y. Cui, *Nano Lett.*, 2012, **12**, 3315.
8 P.-C. Chen, M.-C. Tsai, H.-C. Chen, I. N. Lin, H.-S. Sheu, Y.-S. Lin, J.-G. Duh, H.-T. Chiu and C.-Y. Lee, *J. Mater. Chem.*, 2012, **22**, 5349.
9 Y.-C. Chang, C.-Y. Lee and H.-T. Chiu, *ACS Appl. Mater. Interfaces*, 2014, **6**, 31.
10 K.-C. Hsu, C.-E. Liu, P.-C. Chen, C.-Y. Lee and H.-T. Chiu, *J. Mater. Chem.*, 2012, **22**, 21533.
11 Y. H. Kwon, S.-W. Woo, H.-R. Jung, H. K. Yu, K. Kim, B. H. Oh, S. Ahn, S.-Y. Lee, S.-W. Song, J. Cho, H.-C. Shin and J. Y. Kim, *Adv. Mater.*, 2012, **24**, 5192.
12 M. Armand and J.-M. Tarascon, *Nature*, 2008, **451**, 652.
13 D. Ahn, X. Xiao, Y. Li, A. K. Sachdev, H. W. Park, A. Yu and Z. Chen, *J. Power Sources*, 2012, **212**, 66.
14 M.-S. Park, Y.-M. Kang, G.-X. Wang, S.-X. Dou and H.-K. Liu, *Adv. Funct. Mater.*, 2008, **18**, 455.
15 Y. Wang, J. Y. Lee and H. C. Zeng, *Chem. Mater.*, 2005, **17**, 3899.
16 M. S. Park, G. X. Wang, Y. M. Kang, D. Wexler, S. X. Dou and H. K. Liu, *Angew. Chem.*, 2007, **119**, 764.
17 J. Ning, Q. Dai, T. Jiang, K. Men, D. Liu, N. Xiao, C. Li, D. Li, B. Liu, B. Zou, G. Zou and W. W. Yu, *Langmuir*, 2009, **25**, 1818.
18 C. Wang, Y. Zhou, M. Ge, X. Xu, Z. Zhang and J. Z. Jiang, *J. Am. Chem. Soc.*, 2010, **132**, 46.

19 X. W. Lou, Y. Wang, C. Yuan, J. Y. Lee and L. A. Archer, *Adv. Mater.*, 2006, **18**, 2325.

20 D. Aurbach, E. Zinigrad, Y. Cohen and H. Teller, *Solid State Ionics*, 2002, **148**, 405–416.

21 M. Winter and J. O. Besenhard, *Electrochim. Acta*, 1999, **45**, 31.

22 C.-H. Wang, H.-K. Lin, T.-Y. Ke, T.-J. Palathinkal, N.-H. Tai, I. N. Lin, C.-Y. Lee and H.-T. Chiu, *Chem. Mater.*, 2007, **19**, 3956.

23 C.-H. Huang, Y.-H. Chang, H.-K. Lin, C.-W. Peng, W.-S. Chung, C.-Y. Lee and H.-T. Chiu, *J. Phys. Chem. C*, 2007, **111**, 4138.

24 L. Leibler, *Macromolecules*, 1980, **13**, 1602.

25 M. W. Matsen and F. S. Bates, *Macromolecules*, 1996, **29**, 7641–7644.

26 Joint Committee for Powder Diffraction (JCPDS), File no. 44-1481, File no. 70-4068 and File no. 41-1445, International Center for Diffraction Data, 2002.

27 Reaction-Web, Facility for the Analysis of Chemical Thermodynamics; CRCT, http://www.crct.polymtl.ca.

28 R. Demir-Cakan, Y.-S. Hu, M. Antonietti, J. Maier and M.-M. Titirici, *Chem. Mater.*, 2008, **20**, 1227.

29 X. W. Lou, J. S. Chen, P. Chen and L. A. Archer, *Chem. Mater.*, 2009, **21**, 2868.

30 J. S. Chen, Y. L. Cheah, Y. T. Chen, N. Jayaprakash, S. Madhavi, Y. H. Yang and X. W. Lou, *J. Phys. Chem. C*, 2009, **113**, 20504.

31 J. Lin, Z. Peng, C. Xiang, G. Ruan, Z. Yan, D. Natelson and J. M. Tour, *ACS Nano*, 2013, **7**, 6001.

32 J. M. Haag, G. Pattanaik and M. F. Durstock, *Adv. Mater.*, 2013, **25**, 3238.

33 C.-M. Wang, W. Xu, J. Liu, J.-G. Zhang, L. V. Saraf, B. W. Arey, D. Choi, Z.-G. Yang, J. Xiao, S. Thevuthasan and D. R. Baer, *Nano Lett.*, 2011, **11**, 1874–1880.

34 M. Wachtler, J. O. Besenhard and M. Winter, *J. Power Sources*, 2001, **94**, 189.

35 L. Li, S. Peng, J. Wang, Y. L. Cheah, P. Teh, Y. Ko, C. Wong and M. Srinivasan, *ACS Appl. Mater. Interfaces*, 2012, **4**, 6005.

36 J. Deng, C. Yan, L. Yang, S. Baunack, S. Oswald, H. Wendrock, Y. Mei and O. G. Schmidt, *ACS Nano*, 2013, **7**, 6948–6954.